Electrocatalysis (2019) 10:156–172
https://doi.org/10.1007/s12678-018-0505-z

ORIGINAL RESEARCH

Activity and Durability of Platinum-Based Electrocatalysts with Tin Oxide–Coated Carbon Aerogel Materials as Catalyst Supports

Fabien Labbé[1] · Tristan Asset[2] · Marian Chatenet[1,2,3,4] · Yasser Ahmad[5,6,7] · Katia Guérin[5,6] · Rudolf Metkemeijer[1] · Sandrine Berthon-Fabry[1]

Published online: 15 January 2019
© Springer Science+Business Media, LLC, part of Springer Nature 2019

Abstract

Platinum nanoparticles were deposited onto carbon aerogel with three different tin coatings. The coatings were synthesized at pH = 0.7 or 11.5 and with various masses of $SnCl_2.H_2O$ precursor: 1, 2, and 10 g. The nanoparticles dispersion was found dependent on the morphological properties of the support, i.e., its specific surface, porosity, and coverage by tin oxide. The material electrochemical activity for the oxygen reduction reaction (ORR) and stability was investigated: two accelerated stress tests (ASTs), mimicking either a base-load cycle procedure (P1) or a start-stop procedure (P2), were performed at $T = 80$ °C. The sample coated at pH = 0.7 and the sample with the lowest loading, deposited at pH = 11.5, exhibited interesting performances, both in term of stability (under P1) and activity. On the contrary, samples with highly covering tin oxide coating displayed unsatisfactory initial performances, owing to the low electrical conductivity of their catalytic support. In any case, the aging under P2 leads in a dramatic decrease of the electrocatalyst activity. This either resulted from (i) the low degree of organization of the carbon aerogel, the latter being prone to harsh corrosion when non-covered by the tin oxide, or (ii) by the chemical changes undergone by the tin oxide during the AST, leading to the formation of an amorphous, low electrical conductivity support.

Keywords Carbon aerogel · Tin oxide · Composite · Electrocatalyst · Durability · PEMFC

Introduction

Proton exchange membrane fuel cells (PEMFCs) are energy converters which can be used for automotive, stationary, or nomad applications. These systems produce electrical energy and heat thanks to the electrochemical conversion of hydrogen and oxygen into water. To ensure the viability of this technology, some drawbacks, such as their insufficient durability or high production costs, need to be overcome [1]. Those are mainly linked to the core materials of the PEMFCs. For instance, their insufficient durability is strongly related to the degradation of the electrocatalyst support, especially at the cathode side [2]. These catalytic supports are mainly based on carbon black materials, which are thermodynamically unstable under the usual working conditions of PEMFC cathodes ($T = 80$ °C in humid and acidic environment, cell voltage of 0.6 to 1.0 V) [3–5] and even more in harsh conditions experienced during start-stop procedures or fuel starvation events [6–11]. Theoretically, the carbon corrosion begins with

Electronic supplementary material The online version of this article (https://doi.org/10.1007/s12678-018-0505-z) contains supplementary material, which is available to authorized users.

✉ Sandrine Berthon-Fabry
sandrine.berthon-fabry@mines-paristech.fr

[1] MINES ParisTech, PERSEE-Centre procédés, énergies renouvelables et systèmes énergétiques, PSL University, CS 10207 rue Claude Daunesse, 06904 Sophia Antipolis Cedex, France

[2] Univ. Grenoble Alpes, CNRS, Grenoble INP (Institute of Engineering Univ. Grenoble Alpes) LEPMI, 38000 Grenoble, France

[3] LEPMI, University of Savoie Mont Blanc, 73000 Chambéry, France

[4] French University Institute, Paris, France

[5] Clermont Université, ICCF, F-63000 Clermont-Ferrand, France

[6] CNRS, ICCF, UMR 6296, F-63171 Aubière, France

[7] Fahad Bin Sultan University, P. O Box 15700, Tabuk 71454, Kingdom of Saudi Arabia

the formation of oxygen-containing groups (carboxyl and carbonyl groups, quinone, phenol, and lactone [4, 5, 12]) in the amorphous part of the carbon materials, at the edge of the carbonaceous lattice or in the defects of the carbonaceous crystallographic planes. These groups are then irreversibly transformed into carbon dioxide. Experimentally, the carbon corrosion is observed at $E = 0.9$ V vs. the reversible hydrogen electrode (RHE) [13, 14]. The platinum nanoparticles—the most popular electrocatalyst in PEMFCs—catalyze carbon corrosion [15–17], the later hence starting at potentials as low as $E = 0.6$ V vs. RHE [4, 13–15]. Evidently, several parameters like the working potential [13], the relative humidity [13], the temperature [13, 15, 18–21], and the nature of the gas atmosphere [22] play a role on carbon corrosion and therefore on the alteration of the physicochemical properties of the active layer. Indeed, the formation of oxygen-containing groups onto the carbon surface (i) increases the hydrophilicity of the active layer [4, 5, 12], leading to an increase of the diffusion overpotential [23], and (ii) decreases the electrical conductivity of the catalytic support [24, 25]. Carbon corrosion also modifies the carbon morphology and is prone to trigger the destabilization of the catalyst nanoparticles and the decrease of the electrochemical active surface area (ECSA). These modifications are responsible for a drastic loss of performances of the whole PEMFC system [26]. Several methods are studied to improve the durability of the catalyst support. For instance, other carbon materials were used to substitute carbon blacks, e.g., nanotubes [27, 28], boron-doped diamonds [29], or doped-graphene [30, 31]. These carbon supports exhibited a better resistance towards corrosion phenomena as a result of their graphitic nature (i.e. graphitic carbons are more stable upon corrosion at high potential values [4, 5, 16, 17]). However, some chemical treatments (under HNO_3, H_2SO_4, etc.) were necessary, especially on carbon nanotubes [32–34], to increase the surface hydrophilicity and achieve an acceptable deposition of active material nanoparticles on the carbon surface, as organized carbon areas provide fewer anchoring sites for the latter [35, 36]. Heat treatments were also performed on carbon blacks to improve their degree of the organization [4] (graphitized carbons [5, 12, 37]). Unfortunately, such heat treatments modified the morphology of the carbon blacks by reducing their specific surface area [36], leading to poor quality of the catalyst nanoparticle deposition.

As a matter of fact, none of the methodologies described above enabled to fully stop the carbon corrosion; at best, a high degree of organization slows down the kinetics of the carbon oxidation reaction (COR), at least when potential values above 1 V vs. RHE are experienced [4, 5]. Hence, other studies aimed at modifying the chemical surface of the carbon supports in the hope to find means to further impede the COR. For example, Berthon-Fabry et al. and Asset et al. used fluorination to reduce the kinetics of the corrosion [38, 39]. Because of its high reactivity, elemental fluorine is a very strong oxidizing agent. Its huge reactivity allows its bonding with almost any element, both metals and non-metals. In this case, dangling groups of the structurally disordered carbon materials will preferentially combine with fluorine; this strategy leads to strong covalent C–F bonds, which have been demonstrated less prone to oxidation than C–O bonds, even though again, the COR is not totally suppressed [39]. Others studied carbon phase-free catalyst supports such as conducting polymers [40, 41] and carbides [42–44], or even carbon-free supports like borides [45, 46], metal nitrides [47–49], bi-metal aerogels PtM_x (with M = Ni, Cu, or Co) [50–54], or metal oxides [55–66] have been investigated as catalyst support. Metal oxides have been particularly investigated because of their theoretical stability [3]. For instance, Takabatake et al. studied the initial catalytic activity and the durability of six electrocatalysts Pt/M_yO_x (M = Mo, Nb, Ta, W, Ti, and Sn) for the oxygen reduction reaction (ORR) by rotating disk electrode analysis (RDE) in a 0.1 M $HClO_4$ electrolyte at 25 °C [67]. It turned out that the electrocatalyst deposited on tin oxide, Pt/SnO_2, displays the most encouraging results. Nevertheless, one of the most significant drawbacks of metal oxides for the catalyst support applications is their semi-conductor nature, incompatible with the high electronic conductivity required for electrode support materials [68]. Therefore, other studies focused on doping metal oxides to improve the overall electrical conductivity of the material: many electrocatalysts have been prepared with doped tin oxide (with niobium, antimony, vanadium, and tantalum elements), to probe their initial electrochemical performances and their durability [61, 69–71]. These performances have not always been proved satisfactory because the dopant is gradually depleted from the material's surface leading to pollution and electronic conductivity issues [72, 73]. For this reason, the protection of the carbon surface with a thin (a few nanometers) metal oxides coating, M_yO_x/C, has also been evaluated [74–86] in the hope to create a more resistant composite. This methodology conveys multiple advantages: the M_yO_x/C composites can keep the morphology and the good electrical properties of carbon materials (provided the metal oxide film is indeed thin), thanks to the electrical percolation, and also provide better resistance to the COR owing to the intrinsic thermodynamic stability of the metal oxide. Furthermore, some metal oxides (TiO_2, SnO_2) are expected to stabilize the Pt nanoparticles thanks to the strong metal support interaction (SMSI) effect [87–89]. Encouraging results were generally found for tin oxide–modified carbon supports, SnO_2/C [80, 84–86]. These good electrochemical properties and durability were explained by (i) the stability of the tin dioxide coating and (ii) the modification of the electronic structure of the Pt nanoparticles induced by tin dioxide [86]. Other examples of materials investigated to be used as catalyst support for low-temperature fuel cells are provided in the following reviews [40, 90–94].

In a previous study, the authors have synthesized thin tin oxide coatings on the surface of a wide set of carbon materials (carbon nanotubes, with or without pre-treatment, two different carbon blacks and a home-made carbon aerogel) displaying a large panel of textural, chemical, or structural properties [95]. They studied the influence of different experimental parameters (the pH value of the reactive medium, the amount of tin oxide precursor, and the intrinsic carbon material properties) on the quantity and the quality (homogeneity and covering aspect) of SnO_2 coatings. The mechanisms of tin oxide formation, depending on the pH of the reactive medium, were also discussed. Some of these samples based on carbon aerogel keep an interesting morphology, which opens the way to their use as catalytic supports for the PEMFC application.

In the present work, the authors pursued the effort and synthesized Pt-based electrocatalysts with tin oxide–coated carbon aerogel materials. To this end, Pt nanoparticles of similar individual crystallite sizes were deposited on these new support materials using a modified polyol method [96]. The electrocatalysts were characterized by physicochemical (transmission electron microscopy, X-ray diffraction) and electrochemical (in rotating disk electrode configuration) techniques. Their initial performances towards the oxygen reduction reaction (ORR) and also their durability were compared to those of a benchmark Pt/C electrocatalyst synthesized with the raw carbon aerogel. For this purpose, two accelerated stress tests (ASTs), mimicking either a base-load procedure of PEMFC or the start-stop procedure of PEMFC, were used. In this process, the influence of the quality and quantity of tin oxide coatings on the initial performances and the durability of the electrocatalysts were evaluated and discussed. Finally, the electrochemical performances of the herein-synthesized samples were compared to those obtained using commercial carbon powders as a substrate and a similar polyol synthesis of Pt nanoparticles, already tested in [39].

Experimental

Syntheses

Synthesis of the Raw Carbon Aerogel

The carbon aerogel was synthesized following the Pekala method [97], as described in earlier contributions [38, 98]. Briefly, resorcinol (R: $C_6H_6O_2$, 99%, Alfa Aesar) and formaldehyde (F: CH_2O, 37 wt% in aqueous solution stabilized with 10–15 wt% methanol, Acros Organics) were mixed with the sodium carbonate catalyst (C: Na_2CO_3, 99.9999% metal basis, Sigma-Aldrich) in deionized water with molar ratios F/R = 2, R/C = 300, and 5 wt% solid in solution. The mixture was heated at T = 85 °C for 1 week for gelation and mechanical handling. After several exchanges of the water by acetone, the gel was dried in supercritical CO_2 conditions (80 bars, 37 °C), and the resulting organic aerogel was pyrolyzed at T = 1050 °C under nitrogen flow (1.5 L min^{-1}) into the carbon aerogel sample (CA). After pyrolysis, the carbon aerogel was ground in a mortar for 15 min to obtain a fine powder. All the samples (raw and composites) originate from the same batch.

Synthesis of the Tin Oxide Coating

The objective of this synthesis is to obtain, for comparison purposes, different qualities of tin oxide coatings on the CA surface. Protocols using two different pH values (acidic or basic values) of the reactive medium and quantities of the tin oxide precursor have been used. For the acidic one, the authors followed a protocol proposed initially by Han and Zettl [99]. Firstly, 100 mg of carbon aerogel was mixed in deionized water (400 mL) with a sonotrode (3 × 5 min, 50 W) to improve the dispersion of the carbon materials and break carbon agglomerates. Hydrochloric acid (HCl, 37% reagent grade, Sigma-Aldrich) (7 mL) was added in the solution during the sonication. After that, a predefined quantity of tin chloride ($SnCl_2.2H_2O$, 98%, Alfa Aesar), used as tin oxide precursor was added to the solution, which was mixed at room temperature during 1 h, and then filtered. The filtrate solution was then washed with deionized water until pH ≥ 5. Finally, the obtained powder was dried at T = 90 °C for 6 h under confined atmosphere. For the basic one, the authors used their new protocol, where 5 M sodium hydroxide solution (NaOH, flake, 98%, Alfa Aesar) is progressively added after the sonication, but also after the addition of $SnCl_2.2H_2O$ to maintain a stable basic pH value (pH = 11.5). In this case, no hydrochloric acid HCl was used. More details of these syntheses are given in ref. [95]. The obtained samples are denoted as follows: SnO_x(pH value-quantity of $SnCl_2.2H_2O$)/CA.

Synthesis of Platinum-Based Electrocatalysts

The Pt nanoparticle deposition onto the catalytic support (raw carbon aerogel (CA), or tin oxide–coated carbon aerogel (SnO_2/CA)) used a modified polyol method [96]. Firstly, a colloidal suspension was obtained by reducing a given amount of Pt salt (H_2PtCl_6-xH_2O, 99.9% metal basis, Alfa Aesar) dissolved in a 1:1 volume ethylene glycol (Rotipuran > 99.9%, Roth):ultrapure water solution. The solution was basified (pH = 12.5) and mixed at T = 160 °C at least during 3 h under argon atmosphere. Meanwhile, the chosen catalytic support was mixed in a 1:1 volume ethylene glycol: ultrapure water solution, the quantity of catalytic support being calculated to obtain a final Pt content of 40 wt%. Finally, the two solutions were mixed and the pH adjusted at 3.0 to allow the Pt nanoparticle deposition. The final solution was mixed at least during 12 h, filtered, and washed with ultrapure water. The obtained powder was dried at T = 110 °C for 1 h. The two

Pt/C benchmarks deposited on commercial carbons using the same polyol synthesis for Pt nanoparticle deposition were synthesized and thoroughly characterized in [39]. Briefly, one of the materials was prepared using a high surface area, mildly graphitized, carbon black (ca. 800 $m^2\ g^{-1}$); the corresponding catalyst is labeled Pt/EN; it is loaded at 33 wt% Pt. The other was prepared using a lower surface area strongly graphitized carbon black (ca. 130 $m^2\ g^{-1}$); the corresponding electrocatalyst, labeled Pt/YS, is loaded at 31 wt% Pt.

Material Characterizations

Physicochemical Characterizations

The morphology of different catalyst supports was investigated by *scanning electron microscopy* (SEM) imaging, with a Zeiss® Supra 40 apparatus equipped with a Gemini column operated at 3.00 kV.

Nitrogen sorption analysis was used at 77 K with an ASAP 2020 apparatus (MICROMERITICS). Samples (CA or SnO_2/CA) were first degassed under secondary vacuum at 90 °C for 12 h. The specific surface areas were determined following the Brunauer-Emmett-Teller (BET) model. The Barret-Joyner-Halenda (BJH) method applying to the adsorption branch of the isotherms was used to calculate the pore size distributions [100]. The density functional theory (DFT) model was used to assess the micro-porosity of the different samples. The values are reported by mass of composite.

Transmission electron microscopy (TEM) imaging was used to observe the deposition of the Pt nanoparticles on the different support materials and to evaluate the nanoparticle size dispersion. The apparatus used is a JEOL 2010 microscope with a LaB6 filament, operated at 200 kV, equipped with a retractable SDD Centurio detector. Samples were observed in bright field mode with a point-to-point resolution of 0.19 nm. The obtained micrographs were used to determine the average diameter d_{TEM} and the volume-weighted average diameter d_v (Eq. (1)) of the Pt particles deposited on the different support.

$$d_v = \frac{\sum n_i d_i^4}{\sum n_i d_i^3} \tag{1}$$

where n_i is the number of particles of diameter d_i.

Only isolated and well-defined particles were measured, and a minimum of 100 Pt nanoparticles were counted for each sample.

X-ray diffraction (XRD) measurements were performed using a PANalytical X'Pert pro Philips diffractometer operating at 45 kV and 40 mA using Cu Kα radiation (λ = 0.15418 nm) and a diffracted beam monochromator. The Pt crystallite size was determined from the (111) diffraction peak at 2θ about 39.8° using the Debye-Scherrer equation. As XRD is sensitive to the volume of particles, the crystallite size corresponds to an average volume diameter and must be compared to the volume-weighted average diameter d_v.

To evaluate the quantity of the tin oxide coating in the composites, *thermogravimetric analysis* (TGA) experiments were performed on a TGA-50 apparatus (Shimadzu) with an accuracy of 0.1 mg. The measurements were carried out in the air with a heating rate of 2 °C min^{-1} from room temperature to 600 °C with a 30 min step at T = 600 °C.

Raman spectroscopy was used to probe the carbon structure of the initial bare CA and composites and their aged counterparts after the two ASTs. The spectra were recorded ex situ using a Jobin Yvon T64000 spectrometer with a wavelength LASER excitation of λ = 514 nm. Each sample was analyzed in five different areas. For the sake of comparison, the Raman spectra were normalized to the intensity of the graphitic lattice band ($\nu \approx 1585\ cm^{-1}$). For the carbon materials, five main bands could be detected [4], so spectra were recorded in intervals including these Raman shifts. The obtained curves are used to determine the lateral extension of the graphite planes (hereafter denoted by L_a) following the Knight and White formula [101] (Eq. (2)):

$$L_a = 4.4 \times (A_{Gband}/A_{D1band}) \tag{2}$$

where A_{Gband} and A_{D1band} are, respectively, the area of the G and D1 band.

It turns out that the G and D2 bands are close ($\nu \approx 1585\ cm^{-1}$ and $\nu \approx 1610\ cm^{-1}$, respectively), so curve fitting, using the LabSpec software, was performed to calculate the precise area of the G band. Even if A_{Gband}/A_{D1band} is not proportional to the L_a value for the amorphous carbon materials (it is rather proportional to L_a^2 but no quantitative description of this relationship is provided in the literature) [102, 103], it remains possible to compare the L_a value of the fresh and the aged CAs to evaluate any structural evolution after the two ASTs.

The *electrical conductivity* of the catalyst supports was investigated by a direct resistance measurement at room temperature with a home-made cell. Briefly, a quantity of 50 mg of sample was introduced between two copper electrodes (S_{geo} = 0.7854 cm^2) surrounded by a Teflon ring. Different currents were applied (I = − 105 mA, 105 mA, and 400 mA) by a potentiostat (Biologic HPC-803) at a pressure of $6.37.10^7$ Pa. The voltage value was recorded for each current, and the electrical conductivity (σ) was calculated as an average of the three values obtained with the three currents following Eq. (3):

$$\sigma = e.I/U.S_{geo} \tag{3}$$

where e is the thickness of the sample (cm), I the current applied (A), U the voltage recorded (V), and S_{geo} the surface of the electrode (cm^2).

The Pt content in the electrocatalyst was determined by *atomic absorption spectroscopy* (AAS) (PinAACle 900F, PerkinElmer). To that goal, each electrocatalyst ($m = 5 \pm 1$ mg) was dissolved in 1 mL of a HCl:HNO_3 solution (3:1 volume) at least overnight at $T = 60$ °C. The solution was then diluted with ultrapure water to reach the AAS range for Pt. The Pt content was determined with Syngistixen software, basing on calibration curves obtained by Pt standard solutions. The wavelength considered for Pt was $\lambda = 266$ nm.

Electrochemical Characterizations

Prior to any electrochemical measurement, the glassware was soaked with the concentrated Caro's acid (96% H_2SO_4-30% H_2O_2 mixture) at least overnight, thoroughly rinsed with ultrapure water.

The electrochemical measurements were performed in a four-electrode electrochemical cell using a rotating disk electrode setup. The temperature was controlled using a double envelope. The electrolyte used (0.1 M $HClO_4$) was prepared with ultrapure water and $HClO_4$ (70% Merck Suprapur). The electrochemical characterizations and the ASTs were carried out in two different cells. The working electrode was a rotating disk electrode (RDE) made of glassy carbon ($S_{geo} = 0.196$ cm^2), the counter electrode was a glassy carbon plate, and the reference electrode was a reversible hydrogen electrode (RHE) connected to the cell via a Luggin capillary to limit the Ohmic drop. A Pt wire was connected to the reference electrode with a capacitive bridge to filter the high-frequency electrical noise [104].

The catalytic ink, containing the studied electrocatalysts, was composed of Nafion® (5 wt% perfluorinated-sulfonic acid solution with 15–20 wt% water, Aldrich), ultrapure water and isopropanol (99.5%, Acros Organics). The quantity of Nafion® was normalized by the catalytic support mass to have a ratio equal to 0.3 $g_{Nafion®}\ g_{support}^{-1}$. The solution was ultrasonicated during 15 min to obtain a homogeneous ink, 10 μL of which being deposited on the working electrode: the Pt loading on the electrode was then 20 μg cm$^{-2}_{geo}$.

The electrochemical characterizations were performed at $T = 25$ °C prior to and after the two ASTs. Firstly, the working electrode was immersed in the argon-purged electrolyte at controlled potential $E = 0.40$ V vs. RHE. Then, 50 cyclic voltammetries (CVs) at $\nu = 50$ mV s^{-1}, between 0.05 V vs. RHE and 1.23 V vs. RHE, were performed, following by 3 CVs at $\nu = 20$ mV s^{-1} between 0.05 V vs. RHE and 1.23 V vs. RHE. The Pt-specific surface area (S_{Pt}) was determined by coulometry of the under-potential desorption of H atoms (H_{upd}). For the calculations, the authors assumed that the electrooxidation of a H_{ads} monolayer requires 210 μC cm^{-2}. Finally, the electrolyte was saturated of oxygen, and two CVs were performed at $\nu = 5$ mV s^{-1}, between 1.05 V vs. RHE and 0.20 V vs. RHE at $\omega = 1600$ rpm to evaluate the activity of oxygen reduction reaction (ORR). The latter was expressed in terms of surface ($SA_{0.9}$) and mass ($MA_{0.9}$) activities, determined at $E = 0.90$ V vs. RHE after correction for the Ohmic drop and oxygen mass-transport in a solution.

The two ASTs were performed at $T = 80$ °C to mimic the working conditions of the PEMFCs [105]. They are either a base-load cycle procedure to study the aging of the Pt catalyst (succession of 15,000 cyclic voltammetries under inert atmosphere between $E = 0.6$ V vs. RHE and $E = 1.0$ V vs. RHE at $\nu = 50$ mV s^{-1}, hereafter denoted by "AST P1") or a start-stop procedure to study the aging of the catalyst support (succession of 1000 3-s potential steps under inert atmosphere between $E = 1.0$ V vs. RHE and $E = 1.5$ V vs. RHE, hereafter denoted by "AST P2").

Results and Discussion

Physicochemical Properties of the Catalyst Supports and Platinum-Based Electrocatalysts

Physicochemical Properties of the Catalyst Supports

XRD, X-ray energy-dispersive spectrometry (XEDS), SEM (Fig. 1), N_2 sorption (Fig. 2), and TGA have been carried out on the raw carbon aerogel and on the tin oxide/carbon aerogel composites to probe the influence of the experimental synthesis parameters (pH value of the reactive medium, quantity of tin precursor) on the quality and the quantity of the coating. Their electrical conductivity was also measured. The results of these characterizations are summarized in Table 1.

The raw carbon aerogel (CA) is composed of carbon nanoparticles, with a diameter of 15 ± 5 nm, bound by covalent links leading to the formation of a 3D micro-/meso-/macro-porous material. Whatever the operational parameters, the tin oxide coating (confirmed by XRD and XEDS measurements, not shown here) is visible on the different composites (the surfaces appear rough, which contrasts with the smooth texture of the carbon aerogel). It is formed of nanoparticles with a diameter ca. 5 nm. The values of the textural characteristics (S_{BET}, V_{tot}, and V_{micro}) logically decreased after the coating step (Table 1). The specific surface area evolves from 967 to values around 230 m^2 g^{-1} for the composites, but with a different variation of the porosity/texture. The drop of these specific surface area values is due to the partial filling of the largest pores and the closing of almost all the micropores of the raw carbon aerogel support. Furthermore, it is emphasized owing to the much larger density of tin dioxide

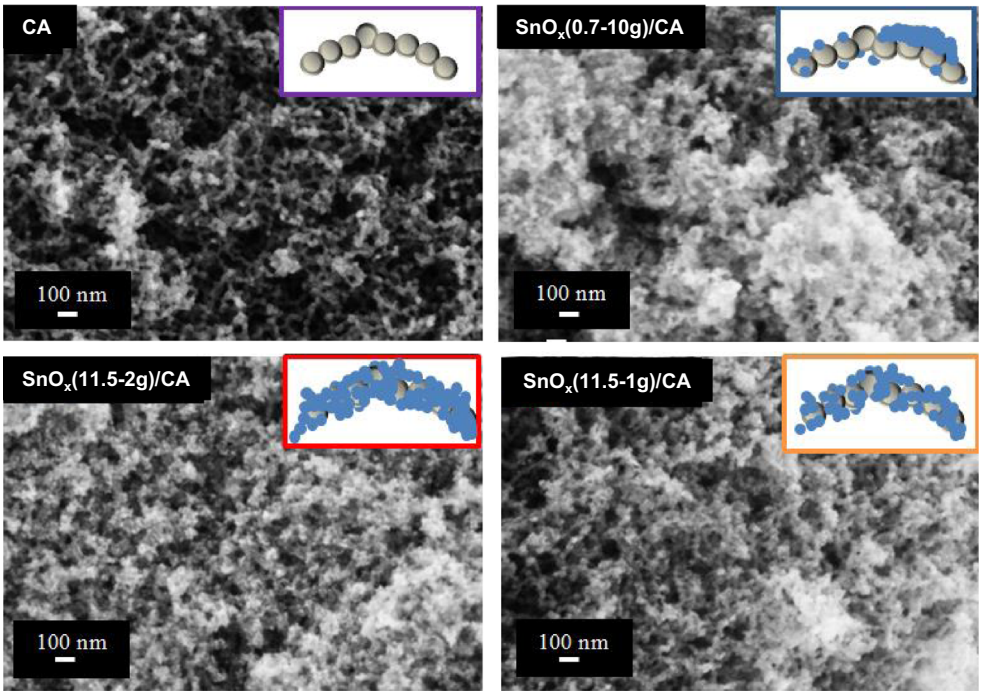

Fig. 1 SEM micrographs and schematic representations (gray: CA and blue: SnO_x) of samples CA, SnO_x(0.7–10 g)/CA, SnO_x(11.5–2 g)/CA, and SnO_x(11.5–1 g)/CA

versus carbon (6.95 g cm^{-3} vs. 2.0 g cm^{-3}). Nevertheless, one can observe some differences between the samples after the coating step. The SnO_x(0.7–10 g)/CA exhibits a heterogeneous and not-covering coating (some parts of carbon surface remain unprotected). This phenomenon logically leads to a low percentage of SnO_x measured by TGA in air (52 wt%), which is assumed as the wt% of the coating. Moreover, few independent aggregates/blocks (up to several micrometers), composed of tin oxide nanoparticles, are observed off the carbon surface on this sample (as previously observed in these synthesis conditions [95]). These blocks are useless and detrimental for the application, because they do not protect the carbon aerogel surface and they would electrically insulate the catalyst nanoparticles from the CA. The two samples, SnO_x(11.5–2 g)/CA and SnO_x(11.5–1 g)/CA, synthesized in basic solution (pH = 11.5), exhibit a good dispersion of tin oxide nanoparticles, in spite of a lower quantity of tin precursor (2 g and 1 g, respectively). The percentages of SnO_x measured by TGA are equal to 81.5 wt% and 64.4 wt%, respectively, logically explained by the difference of the quantity of tin precursor. Considering a totally covering coating of the tin dioxide nanoparticles (with a diameter equal to 5 nm), the theoretical percentage of the coating value is about 95 wt%. So, the sample SnO_x(11.5–2 g)/CA exhibits an interesting and significant coating (81.5 wt%) with a visible porosity and interesting S_{BET} and V_{tot} values (225 m^2 g^{-1} and 0.56 cm^3 g^{-1}) for the application. The coating of the sample SnO_x(11.5–1 g)/CA is correct but limited by the lower quantity of tin precursor. No detrimental SnO_x independent blocks are observed for these two samples. The differences observed between sample synthesized in acidic (pH = 0.7) and basic (pH = 11.5) solution are the consequences of electrostatic interactions (repulsion for samples synthesized in acidic condition or attraction for samples synthesized in basic condition) between the reactive species and the CA surface [95]. That is why the percentages of SnO_x measured by TGA are higher for the samples SnO_x(11.5–2 g)/CA and SnO_x(11.5–1 g)/CA than the percentage of the sample SnO_x(0.7–10 g)/CA, even though lower tin precursor contents had been used.

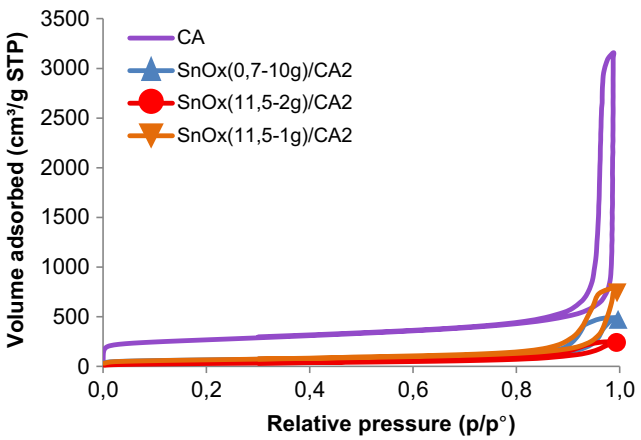

Fig. 2 Nitrogen adsorption isotherms of samples CA, SnO_x(0.7–10 g)/CA, SnO_x(11.5–2 g)/CA, and SnO_x(11.5–1 g)/CA, measured at 77 K after an outgassing under secondary vacuum at 90 °C

Not only the quantity, but also the quality of the tin oxide coatings, has a major influence on the electrical conductivity values σ of the samples (composites dried

Table 1 Physicochemical characteristics of the samples synthesized. The S_{BET}, V_{tot}, V_{meso}, and V_{micro} are reported by mass of composite

Sample	S_{BET} [a] ($m^2\ g^{-1}$)	V_{tot} [b] ($cm^3\ g^{-1}$)	V_{meso} [b] ($cm^3\ g^{-1}$)	V_{micro} [b] ($cm^3\ g^{-1}$)	SnO_x [c] (wt%)	σ [d] (S cm^{-1})
CA	967 ± 24	4.88 ± 0.05	0.54 ± 0.05	0.20 ± 0.01	0.0 ± 0.1	2.2 ± 0.3
SnO_x(0.7–10 g)/CA	236 ± 6	0.76 ± 0.05	0.46 ± 0.05	0.05 ± 0.01	52.5 ± 0.8	1.3 ± 0.1
SnO_x(11.5–2 g)/CA	225 ± 6	0.56 ± 0.05	0.30 ± 0.05	0.00 ± 0.01	81.5 ± 0.8	0.2 ± 0.1
SnO_x(11.5–1 g)/CA	234 ± 6	1.22 ± 0,05	0.40 ± 0.05	0.03 ± 0,01	64.4 ± 1.1	0.5 ± 0.1

[a] S_{BET} BET surface area

[b] V_{tot}, V_{meso}, and V_{micro} the total porous volume, mesoporous volume, and microporous volume, respectively

[c] SnO_x (wt%) the wt% of SnO_x measured after the TGA analyses

[d] σ electrical conductivity values

at 90 °C in air without any further calcination). For example, the higher the quantity of coating, the lower the electrical conductivity value σ. The more or less pronounced presence of tin dioxide (a semi-conductor material: band gap about 3.5 eV [68]) explains this phenomenon. Furthermore, the sample SnO_x(0.7–10 g)/CA exhibits a heterogeneous and non-covering coating with plenty of uncovered areas of carbon aerogel surface, which are enough to allow fast transfer of electrons (small contact resistance): this sample has the highest electrical conductivity value of the composites, but exposes unprotected areas of the CA.

Physicochemical Properties of Platinum-Based Electrocatalysts

The different electrocatalysts synthesized from the raw carbon aerogel and the tin oxide/carbon aerogel composites are analyzed by TEM. The pictures and the Pt nanoparticle size distribution are given in Fig. 3. The XRD diffractograms, plotted for the four electrocatalysts, are shown in Fig. 4. Moreover, the Pt content (calculated with AAS), the average diameter of the Pt d_{TEM}, and the volume-weighted average diameter d_v (calculated from TEM pictures) and the average size of Pt nanocrystallites (d_{XDR}, calculated with the Debye-Scherrer equation from the (111) diffraction peak at 2θ about 39.8°) are given in the Table 2.

Whatever the catalyst support, the deposition of Pt Nanoparticles is obvious (Figs. 3 and 4). Slight differences in d_{XRD} are observed for the various supports values. This agrees with the colloidal method used for their synthesis (samples coming from the same colloidal suspension): apart from different degrees of agglomeration for different supports, the crystallite sizes should remain essentially identical. Differences between d_v and d_{XRD} could be observed. The high values of d_v could be explained by the agglomerations of platinum nanoparticles, which are relatively abundant in the electrocatalysts Pt/SnO_x(0.7–10 g)/CA and Pt/SnO_x(11.5–2 g)/CA. Moreover, it is possible to have

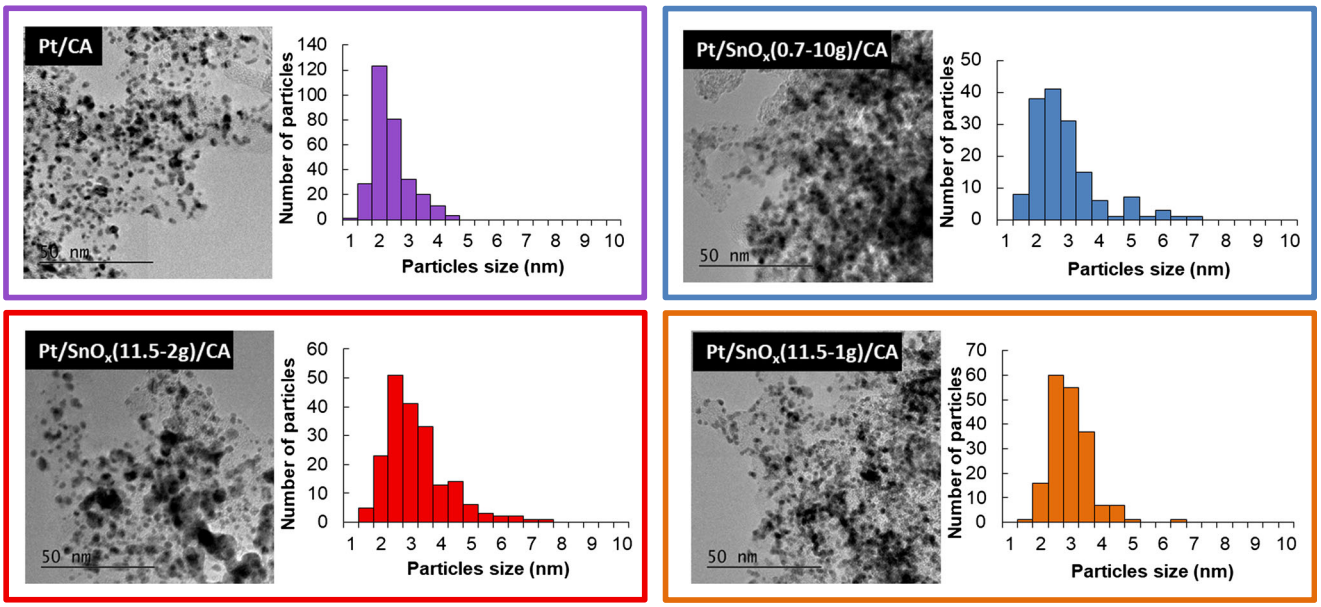

Fig. 3 TEM pictures and Pt nanoparticle size distribution of Pt/CA, Pt/SnO_x(0.7–10 g)/CA, Pt/SnO_x(11.5–2 g)/ CA, and Pt/SnO_x(11.5–1 g)/CA

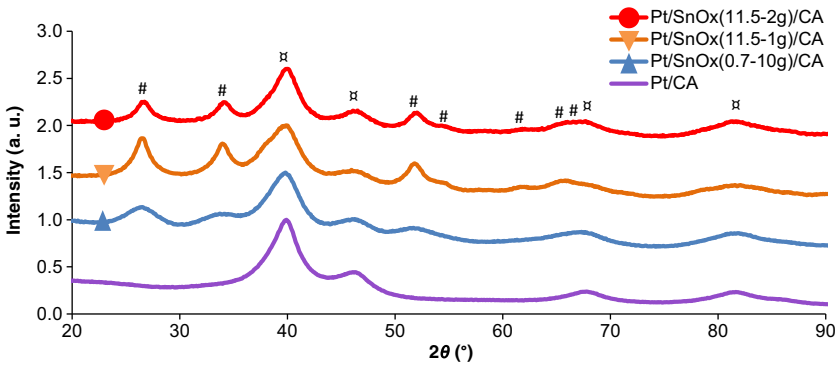

Fig. 4 XRD diffractograms of Pt/CA, Pt/SnO_x(0.7–10 g)/CA, Pt/SnO_x(11.5–2 g)/CA, and Pt/SnO_x(11.5–1 g)/CA electrocatalysts. The number sign and currency sign correspond to the visible peaks of the crystallographic plans of SnO_2 and Pt, respectively

some small nanoparticles (with a diameter lower than or equal to 1 nm), which are not distinguishable from the background by image analysis, leading to d_v values oversized. For the electrocatalyst based on the raw carbon aerogel (Pt/CA), the deposition of the Pt Nanoparticles is homogeneous with a narrow size distribution, centered on 2.1 nm. The carbon aerogel, with its low organized structure and its high specific surface area (967 $m^2\ g^{-1}$), displays a lot of anchoring sites for the nanoparticles. For the electrocatalysts based on the tin oxide–coated carbon aerogel (Pt/SnO_x/CA), the Pt nanoparticle distributions are wider, with a tendency to gather Pt nanoparticles, as a result of larger degree of agglomeration of individual crystallites. This phenomenon is accompanied by non-negligible Pt nanoparticle agglomeration [106, 107] and can be explained by two main factors. The less pronounced porosity of the SnO_x/CA supports leads to lower specific surface area values (between 225 and 236 $m^2\ g^{-1}$) and to less anchoring site for the Pt nanoparticles. Moreover, the quantity and the quality of the coating have also a major influence on the Pt nanoparticle deposition. Although the SnO_x(11.5–2 g)/CA support has the more homogeneous and the more covering coating, the Pt/SnO_x(11.5–2 g)/CA electrocatalyst displays a mediocre Pt dispersion with a significant number of Pt agglomerates. This could be explained by the different interactions between, on the one hand, Pt and carbon and, on the other hand, Pt and tin dioxide [87, 108]. In the second case, Pt tends to agglomerate, as already observed by Cognard et al., on the tin dioxide supports. This phenomenon was observed on non-doped tin dioxide supports, as well as on doped (with niobium or antimony elements) supports [71–73]. In other words, not only the textural characteristics, but also the chemical nature of the catalyst support, have a direct influence on the quality of the Pt nanoparticles deposited. Finally, the morphologies, in terms of distribution, of the Pt/EN and Pt/YS samples are very close to those monitored for Pt/CA (see [39] for details).

Electrochemical and Physicochemical Characterizations after the Load Cycle Procedure of Accelerated Stress Tests (AST P1)

The four Pt-based electrocatalysts were tested electrochemically, firstly in argon-saturated electrolyte and then in oxygen-saturated electrolyte to measure their ORR activity. These characterizations were performed prior to and after the AST P1, mimicking a base-load cycle procedure. The CVs curves plotted are given in Figs. 5 and 6. Physicochemical characterizations (TEM (Fig. 7) and Raman spectroscopy) were also performed at the end of AST P1, to probe the changes of the Pt nanoparticles and of the catalytic support, as summarized in Table 3. The determination of the specific surface after the AST P1 and P2 was not performed for all electrocatalysts (as well as the specific activity at 0.9 V vs. RHE). Indeed, the specific surface was determined from the H_{upd} region, using the capacitive current in the 0.4–0.6 V vs. RHE as a

Table 2 Physicochemical characteristics of the four electrocatalysts

Samples	Pt content (wt%—AAS)	d_{TEM}[a] (nm)	d_v[b] (nm)	d_{XRD}[c] (nm)
Pt/CA	36.8 ± 0.1	2.1 ± 0.6	2.7 ± 0.6	2.4 ± 0.2
Pt/SnO_x(0.7–10 g)/CA	27.8 ± 0.1	2.6 ± 1.0	3.8 ± 1.0	2.4 ± 0.2
Pt/SnO_x(11.5–2 g)/CA	34.5 ± 0.1	3.0 ± 1.0	3.8 ± 1.4	2.6 ± 0.2
Pt/SnO_x(11.5–1 g)/CA	27.1 ± 0.1	2.7 ± 0.7	3.1 ± 0.7	2.0 ± 0.2

[a] d_{TEM} the average size of the Pt nanoparticles

[b] d_v the volume-weighted average diameter calculated from TEM pictures

[c] d_{XRD} the average size of Pt nanocrystallites determined from the (111) diffraction peak using the Debye-Scherrer equation

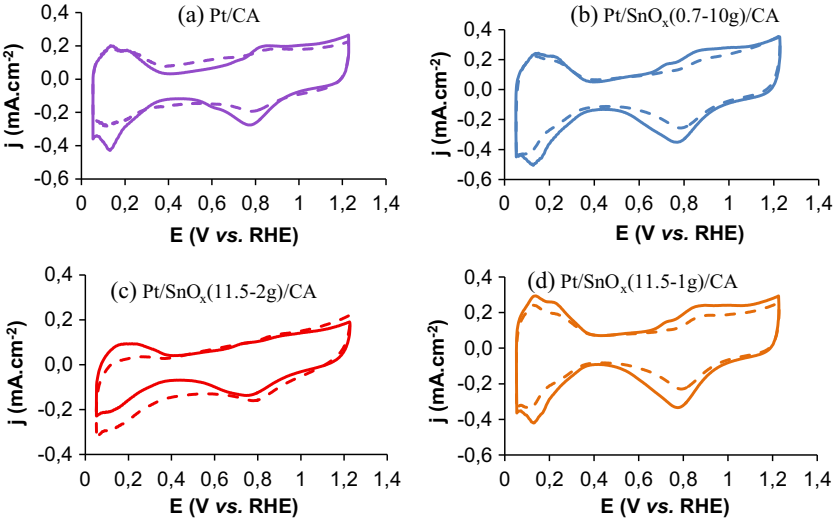

Fig. 5 **a**–**d** Representative cyclic voltammograms in argon-purged electrolyte (0.1 M $HClO_4$, scan rate $v = 20$ mV s^{-1}) at $T = 25$ °C of the Pt-based electrocatalysts prior to (fresh, full lines) and after (dotted lines) AST P1 (succession of 15,000 cyclic voltammetries under inert atmosphere between $E = 0.6$ V vs. RHE and $E = 1.0$ V vs. RHE at $v = 50$ mV s^{-1}, in 0.1 M $HClO_4$ at $T = 80$ °C)

baseline to precisely determine the charge under the H_{upd} peak. During the aging, the formation of a quinone-hydroquinone peak (due to the partial corrosion of the carbon) was often observed, hence modifying the baseline (possibly without any change of the H_{upd}) and resulting in an underestimation of the H_{upd} (this is likely very much the case for Pt/CA, and in a lesser extent for Pt/SnO_x11.5–2 g)/CA, for which the capacitive current strongly evolves after aging). To avoid any misinterpretation of the results, we thus decided to comment the evolution of the specific surface areas in a qualitative manner.

The cyclic voltammograms obtained in an argon-saturated electrolyte (Fig. 5) display a classical behavior with the absorption/desorption of the proton H^+ at low working potentials ($E < 0.4$ V vs. RHE). The evolution of the electrochemical behavior of the electrocatalysts depends on the catalytic support. The double-layer capacitance ($0.4 < E < 0.6$ vs. RHE) evolves, as a consequence of the formation of new oxygen-containing groups, which initiate the carbon corrosion mechanism into CO_2, thereby destroying the carbon support and leading to increased diffusion overpotential in systems [22]. The degradation of the carbon aerogel is confirmed by the evolution of the L_a values (from 0.8 to 3.3 nm), signing the irreversible corrosion of the amorphous regions of the CA, leaving only (at least at that stage of the process) the more graphitic regions of the material (hence, the increase of L_a). Such carbon degradation favors the loss of some Pt nanoparticles. The Pt nanoparticles supported on the raw carbon aerogel are also subjected to the Ostwald ripening mechanism during AST P1 (broadening of the particle size dispersion, an increase of the average diameter, and keeping the spherical shapes of the nanoparticles [109], Fig. 7). The decrease of $MA_{0.9}$ (ca. 54%) is directly linked to these two phenomena. Overall, the carbon-related degradation of Pt/CA under P1 AST is more important than what witnessed for more graphitic carbons (Pt/EN and more specifically Pt/YS), as detailed in [39] and recalled in supporting information (Table SI-1), whereas

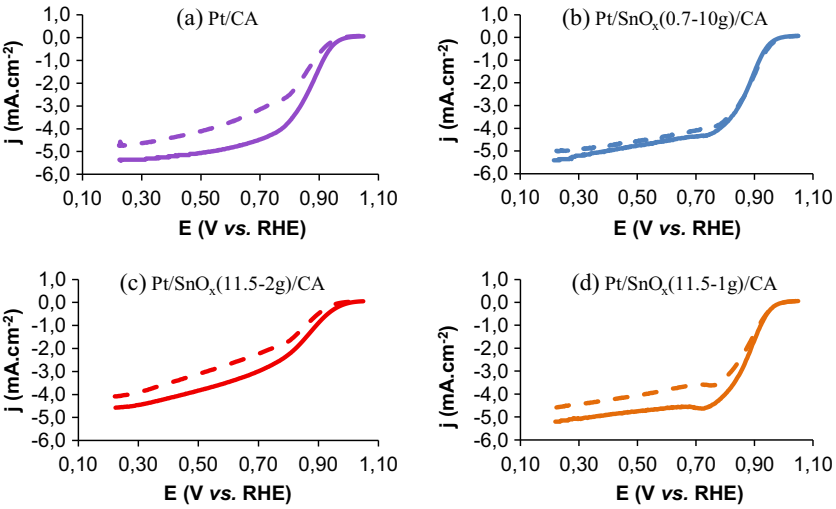

Fig. 6 **a**–**d** Representative ORR cyclic voltammograms at $T =$ 25 °C of the Pt-based electrocatalysts prior to (fresh, full lines) and after (dotted lines) AST P1 (succession of 15,000 cycles)

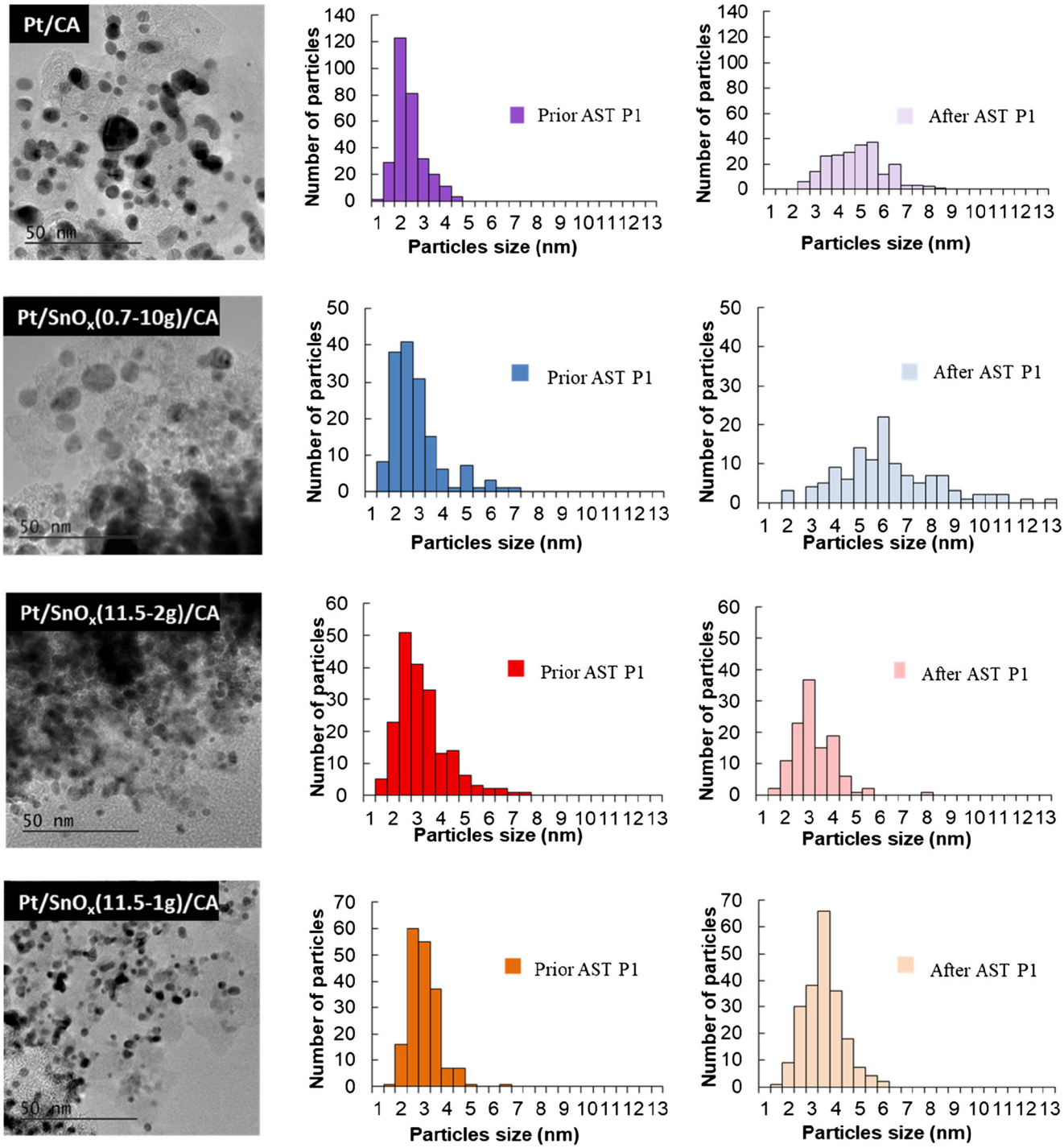

Fig. 7 Representative TEM micrographs obtained after AST P1 and corresponding Pt nanoparticle size distribution of the Pt-based electrocatalysts prior to and after AST P1 (succession of 15,000 cycles)

its initial performances ($SA_{0.90}$, $M_{0.90}$) are intermediate (this phenomenon being induced by the agglomerated nanoparticles observed on Pt/CA and, to a larger extent, Pt/YS (see [39]).

The Pt/SnO_x(0.7–10 g)/CA and Pt/SnO_x(11.5–1 g)/CA exhibit a slight decrease in S_{Pt} during the AST P1 (ca. 20%, see Table 3). The presence of the tin oxide seems to limit the degradation of the carbon aerogel (no evolution of the double-layer capacitance and the L_a ini and L_a fin values are similar, Table 3), resulting in more stable catalytic supports. The loss of S_{Pt} for Pt/SnO_x(0.7–10 g)/CA could be explained by the drastic increase of the average Pt nanoparticle size, leading to an increase of the surface activity ($SA_{0.9}$ increases from 204.8 to 286.7 μA cm_{Pt}^{-2}). On the contrary, the particle

Table 3 Summary of the kinetic parameters extracted from the ORR cyclic voltammograms and physicochemical properties of the Pt-based electrocatalysts prior to and after AST P1

Sample	S_{Pt} ini[a] ($m^2\ g_{Pt}^{-1}$)	S_{Pt} fin[a] ($m^2\ g_{Pt}^{-1}$)	$SA_{0.9}$ ini[b] ($\mu A\ cm_{Pt}^{-2}$)	$SA_{0.9}$ fin[b] ($\mu A\ cm_{Pt}^{-2}$)	$MA_{0.9}$ ini[c] ($A\ g_{Pt}^{-1}$)	$MA_{0.9}$ fin[c] ($A\ g_{Pt}^{-1}$)	d_{TEM} ini[d] (nm)	d_{TEM} fin[d] (nm)	L_a ini[e] (nm)	L_a fin[e] (nm)
Pt/CA	41.1	–	224	–	92.0	42.5	2.1	4.5	0.8	3.3
Pt/SnO_x(0.7–10 g)/CA	51.8	42.4	205	287	106	121	2.6	5.9	1.7	1.7
Pt/SnO_x(11.5–2 g)/CA	22.1	–	216	–	55.7	27.4	3.0	2.9	1.9	1.9
Pt/SnO_x(11.5–1 g)/CA	54.1	44	221	223	119	98	2.7	3.2	1.7	1.7

[a] S_{Pt} ini and S_{Pt} fin depict the initial and final Pt-specific surface area, respectively

[b] $SA_{0.9}$ ini and $SA_{0.9}$ fin depict the initial and final surface activity measured at $E = 0.90$ V vs. RHE, respectively

[c] $MA_{0.9}$ ini and $MA_{0.9}$ fin depict the initial and final mass activity measured at $E = 0.90$ V vs. RHE, respectively

[d] d_{TEM} ini and d_{TEM} fin depict the initial and final average size of the Pt nanoparticles, respectively

[e] L_a ini and L_a fin depict the initial and final lateral extension of the graphite planes

size distribution of Pt/SnO_x(11.5–1 g)/CA displays a little offset to bigger sizes (Fig. 7). This sample also exhibits similar initial and final catalytic activities (Table 3). In this case, the coating seems to improve the behavior of the electrocatalyst (stability of the Pt nanoparticles and protection of the support). Finally, the Pt/SnO_x(11.5–2 g)/CA electrocatalyst exhibits a low S_{Pt} ini value compared to the other samples, which could be explained by the mediocre disposition of the Pt (Fig. 3) and most importantly by the low electrical conductivity of the support (0.2 ± 0.1 S cm^{-1}). In that case, the homogeneous and covering tin oxide coating (Table 1) seems to insulate a significant number of Pt particles from the CA support, this phenomenon explaining the low initial value of mass activity $MA_{0.9}$ ini (55.7 A g_{Pt}^{-1}) and why there is no or very little change of the Pt particle size distribution (Fig. 7).

To conclude, the presence of the tin oxide coating can be either beneficial or detrimental to the catalytic performances of the Pt-based electrocatalysts in AST P1, depending on the original "morphology" of the Pt/SnO_x/CA sample. While the sample Pt/SnO_x(11.5–1 g)/CA exhibits promising performances and durability (its CA surface is only partially covered by the SnO_2 deposit), samples where the CA surface is totally covered by SnO_2 exhibit unsatisfactory initial catalytic performances, because of the low electrical conductivity values of the support material.

Electrochemical and Physicochemical Characterizations after the Start-Stop Procedure of Accelerated Stress Tests (AST P2)

Finally, the Pt-based electrocatalysts were tested electrochemically under the AST P2, which mimics the frequent start-stops that can be experienced in automotive applications. As previously, the samples were tested in argon-saturated electrolyte and then in oxygen-saturated electrolyte, both prior to and after the AST P2. The corresponding CVs are given in the Figs. 8 and 9, respectively. Physicochemical characterizations (TEM (Fig. 10) and Raman spectroscopy) were also performed at the end of AST P2 (Table 4).

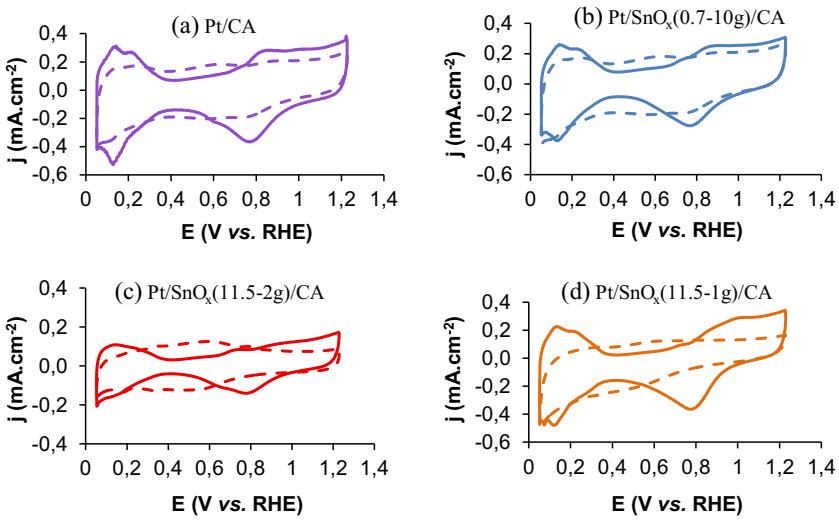

Fig. 8 **a**–**d** Representative cyclic voltammograms in argon-purged electrolyte (0.1 M $HClO_4$) at T = 25 °C of the Pt-based electrocatalysts prior to (fresh, full lines) and after (dotted lines) AST P2 (succession of 1000 3-s potential steps under inert atmosphere between $E = 1.0$ V vs. RHE and $E = 1.5$ V vs. RHE, in 0.1 M $HClO_4$ at $T = 80$ °C)

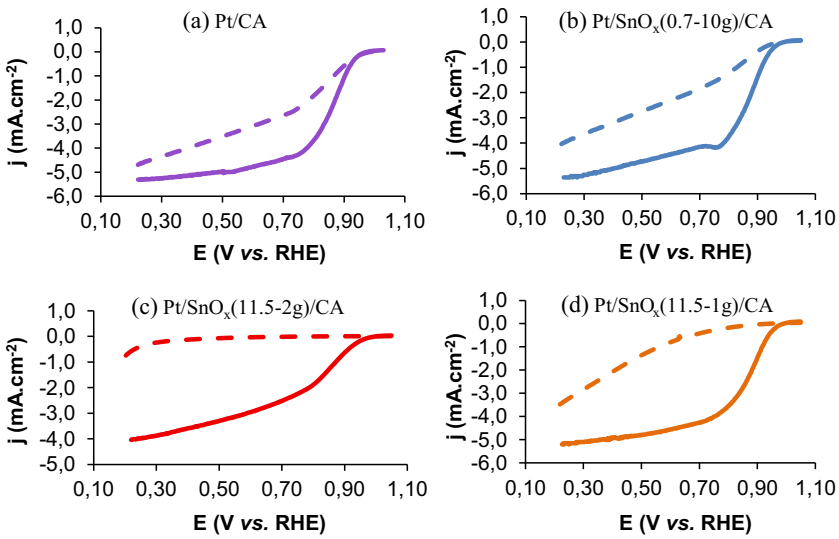

Fig. 9 **a**–**d** Representative ORR cyclic voltammograms at T = 25 °C of the Pt-based electrocatalysts prior to (fresh, full lines) and after (dotted lines) AST P2 (succession of 1000 cycles)

The cyclic voltammograms obtained in argon-saturated electrolyte (Fig. 8) evolve a lot upon AST P2, which is the consequence of a severe degradation of the catalytic support. The H_{upd} features (hence, the specific surface area of Pt) partially disappear for Pt/CA and Pt/SnO_x(0.7–10 g)/CA and are completely suppressed for Pt/SnO_x(11.5–2 g)/CA and Pt/SnO_x(11.5–1 g)/CA. Furthermore, samples synthesized with raw carbon aerogel (Pt/CA) or with the heterogeneous and non-covering tin oxide coating (Pt/SnO_x(0.7–10 g)/CA) display a significant enlargement of their double-layer capacitance, characteristic of the formation of oxygen-containing groups at the available carbon surface. The appearance of the oxidation peak relative to the quinone into hydroquinone transformation at $E \approx 0.6$ V vs. RHE [4] is another indicator of the formations of these new functional groups. The harmful effect of these groups for the catalytic support for the PEMFC application was previously discussed in this study. As a result, at the end of AST P2, the raw CA support is heavily degraded, in line with the increase of the L_a value (from 0.8 to 1.8 nm): the amorphous carbon firstly corrodes (leading to an apparent increase of L_a), but then the organized parts of the CA also degrade in these conditions (later), leading to a further decrease of L_a. Overall, these degradations lead to the detachment of a significant number of Pt nanoparticles from the CA, further explaining the considerable drop of the mass activity (about 71%), this latter value being calculated with respect to the initial mass of Pt contained in the sample.

The Pt/SnO_x(0.7–10 g)/CA electrocatalyst exhibits a similar percentage of loss of $MA_{0.9}$ than Pt/CA. The plentiful uncovered surface areas of the carbon seem to undergo the same degradations as for the bare Pt/CA. In these conditions, the tin oxide coating has no beneficial effect on the durability of the catalytic support. The Pt/SnO_x(11.5–2 g)/CA and Pt/SnO_x(11.5–1 g)/CA samples also display visible changes of the double-layer capacitance after AST P2, especially for Pt/SnO_x(11.5–2 g)/CA. In this case, one can wonder if the tin oxide coatings were also modified under the very oxidizing conditions of AST P2. The similar values of the L_a ini and L_a fin obtained for the two samples (Table 4) seem to indicate a relative stability of the carbon aerogel, though, probably because no CA is directly exposed to the electrolyte. This apparent stability must, however, not be understood as a positive effect. Indeed, as stated above, the tin oxide deposit seems strongly modified. This assumption is corroborated by the drastic loss of the mass activity (and of specific surface, as evidenced by the disappearance of the H_{upd}) when no change of Pt particle size is observed. The alteration of tin oxide catalytic supports was already observed by Cognard et al. [73]: some dissolution of tin in argon-purged 0.1 M electrolyte at T = 57 °C after a holding of the disk potential at E = 1.2 V vs. RHE for 30 min using rotating disk and rotating ring-disk electrode was noticed. According to the authors, such tin oxide dissolution leads to the formation of an amorphous layer with a low electrical conductivity at the surface of the samples. In the present case, this transformation could lead to an electrical disconnection of the Pt nanoparticles, this likely causing the drastic drop of $MA_{0.9}$ for Pt/SnO_x(11.5–2 g)/CA and Pt/SnO_x(11.51 g)/CA noted in Table 4.

Finally, after AST P2, the Pt/CA sample exhibits a broader Pt nanoparticle size distribution histogram, with a shift towards bigger sizes (Fig. 10). Thus, for this sample, the degradation of the raw CA support is likely coupled with some Ostwald ripening. This is not observed for the tin oxide–coated CAs (Fig. 10), the difference being tentatively explained by the electrical

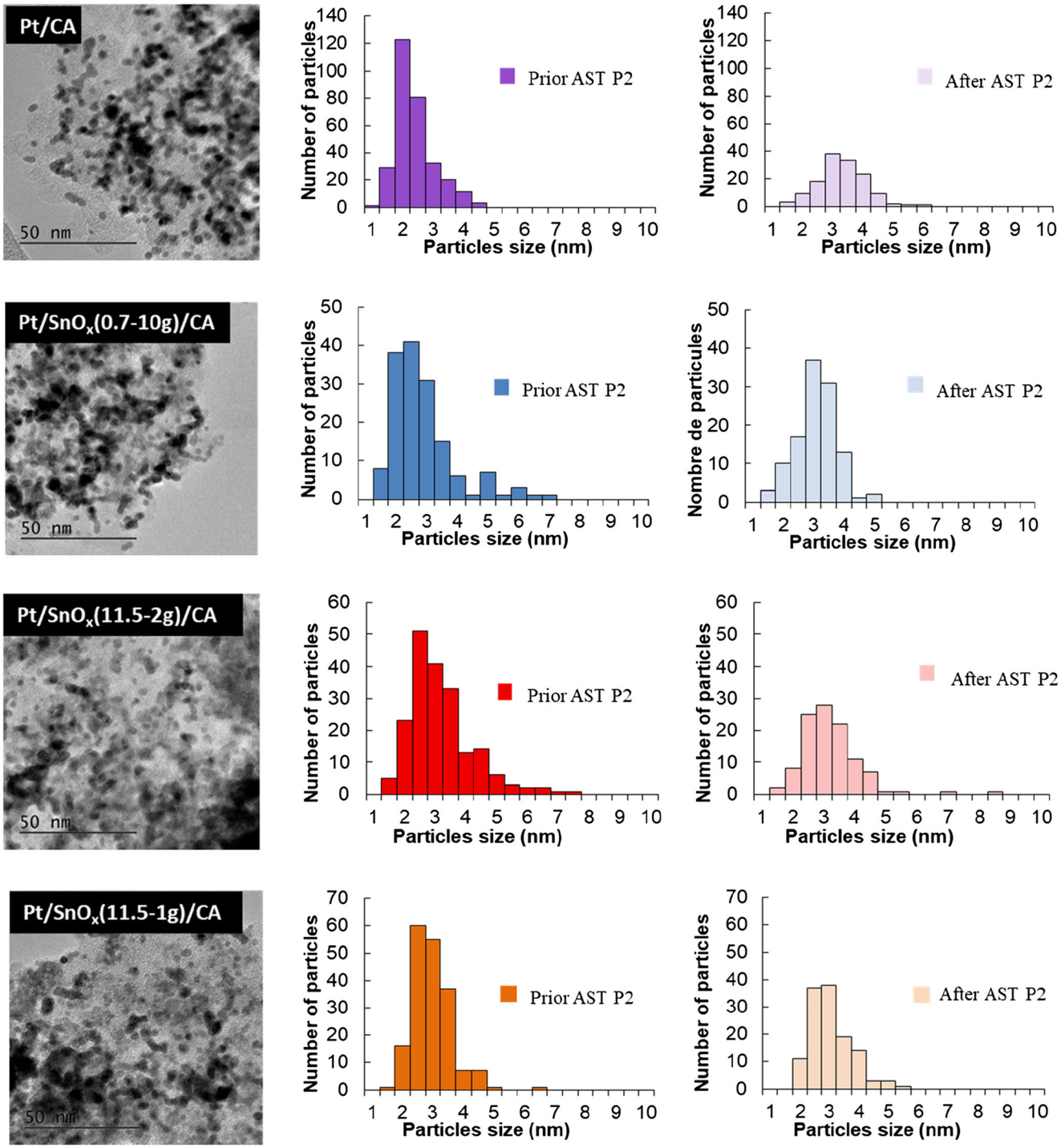

Fig. 10 Representative TEM micrographs obtained after AST P2 and corresponding Pt nanoparticle size distribution histograms of the Pt-based electrocatalysts prior to and after the 1000 cycles of AST P2

disconnection of the Pt nanoparticles discussed previously for these samples. In comparison, it seems that having a more graphitized carbon support like YS (see Table SI-1) results in a slightly higher (if not similar) durability in start-stop conditions, the HSAC support (Pt/EN) suffering from higher degradation.

Conclusion

Several tin oxide coatings were synthesized by impregnation and dried at 90 °C on the surface of a carbon aerogel to improve the durability of this catalytic support under the working conditions of a PEMFC. The influence of the quantity and

Table 4 Summary of the kinetic parameters extracted from the ORR cyclic voltammetries and physicochemical properties of the Pt-based electrocatalysts prior to and after the 1000 cycles of AST P2

Sample	S_{Pt} ini[a] ($m^2\ g_{Pt}^{-1}$)	$SA_{0.9}$ ini[b] ($\mu A\ cm_{Pt}^{-2}$)	$MA_{0.9}$ ini[c] ($A\ g_{Pt}^{-1}$)	$MA_{0.9}$ fin[c] ($A\ g_{Pt}^{-1}$)	d_{TEM} ini[d] (nm)	d_{TEM} fin[d] (nm)	L_a ini[e] (nm)	L_a fin[e] (nm)
Pt/CA	64.2	174	126	32.6	2.1	3.0	0.8	1.8
Pt/SnO_x(0.7–10 g)/CA	50.9	183	93.3	20.4	2.6	2.8	1.7	1.9
Pt/SnO_x(11.5–2 g)/CA	19.6	188	36.9	0.3	3.0	2.9	1.9	1.9
Pt/SnO_x(11.5–1 g)/CA	48.8	209	102	1.7	2.7	2.8	1.7	1.8

[a] S_{Pt} ini depict the initial Pt-specific surface area

[b] $SA_{0.9}$ ini depict the initial surface activity measured at $E = 0.90$ V vs. RHE

[c] $MA_{0.9}$ ini and $MA_{0.9}$ fin depict the initial and final mass activity measured at $E = 0.90$ V vs. RHE, respectively

[d] d_{TEM} ini and d_{TEM} fin depict the initial and final average size of the Pt nanoparticles, respectively

[e] L_a ini and L_a fin depict the initial and final lateral extension of the graphite planes

quality (homogeneity and covering aspect) of this coating on the Pt nanoparticle depositions, their catalytic performances towards the oxygen reduction reaction, and the durability of the electrocatalysts were studied for two accelerated stress tests procedures, one mimicking a base-load cycling (AST P1) and the other a start-stop procedure (AST P2). It turns out that the not only textural characteristics of the composite (especially the porosity and the specific surface area), but also the chemical nature (the Pt nanoparticles, tend to agglomerate on the tin oxide surface) of the catalyst support have a direct influence on the Pt nanoparticle deposition. At the end of AST P1, some coatings lead to an improvement of the durability of the electrocatalysts: for example, the Pt/SnO_x(11.5–1 g)/CA sample exhibits interesting initial performances, a good durability of the catalytic support, and stable Pt nanoparticles. Nevertheless, if the carbon surface is totally covered, the initial catalytic performances are unsatisfactory, because of the low electrical conductivity value of the catalytic support. Finally, all electrocatalysts exhibit significant degradations after AST P2, leading to a severe drop of the catalytic activity. It could be explained either by the degradation, under the harsh experimental conditions of AST P2, of the uncovered carbon surface areas or by the alteration of the tin oxide coating, resulting in the formation of an amorphous layer with a low electrical conductivity, thereby disconnecting a significant number of Pt nanoparticles. As a result, the real beneficial interest of tin oxide coating to protect carbon supports is still open to question, hence requesting investigation with different carbon supports, as YS or EN.

Acknowledgements The authors wish to thank Pierre Ilbizian for the help with supercritical drying, Suzanne Jacomet for the SEM analysis, Gabriel Monge for the XRD (CEMEF-MINES ParisTech), and Capenergies and Tenerrdis for their support. MC thanks the French IUF for its support.

Funding Information The French National Research Agency program, (ANR-14-CE05-0047 project CORECAT) funded this work. Some of this work has also been funded within the framework of the Centre of Excellence of Multifunctional Architectured Materials "CEMAM" n° AN-10-LABX-44-01.

Publisher's Note Springer Nature remains neutral with regard to jurisdictional claims in published maps and institutional affiliations.

References

1. Department of Energy (DoE), Fuel cell technologies office multi-year research, development, and demonstration - plan section 3.4 fuel cells section (2016)
2. J. Wu, X. Zi, J.J. Martin, H. Wang, J. Zhang, J. Shen, S. Wu, W. Merida, A review of PEM fuel cell durability: degradation mechanisms and mitigation strategies. J. Power Sources **184**(1), 104–119 (2008)
3. K. Sasaki, F. Takasaki, Z. Noda, S. Hayashi, Y. Shiratori, K. Ito, Alternative electrocatalyst support materials for polymer electrolyte fuel cells. Polym. Electrolyte Fuel Cells **10 Pts 1 2 33**, 473 (2010)
4. L. Castanheira, L. Dubau, M. Mermoux, G. Berthome, N. Caque, E. Rossinot, M. Chatenet, Carbon corrosion in proton-exchange membrane fuel cells: from model experiments to real-life operation in membrane electrode assemblies. ACS Catal. **4**(7), 2258–2267 (2014)
5. L. Castanheira, W.O. Silva, F.H.B. Lima, A. Crisci, L. Dubau, F. Maillard, Carbon corrosion in proton-exchange membrane fuel cells: effect of the carbon structure, the degradation protocol, and the gas atmosphere. ACS Catal. **5**(4), 2184–2194 (2015)
6. A. Taniguchi, T. Akita, K. Yasuda, Y. Miyazaki, Analysis of electrocatalyst degradation in PEMFC caused by cell reversal during fuel starvation. J. Power Sources **130**(1–2), 42–49 (2004)
7. F.A. De Bruijn, V.A.T. Dam, G.J.M. Janssen, Review: durability and degradation issues of PEM fuel cell components. Fuel Cells **8**, 3 (2008)
8. J. Durst, A. Lamibrac, F. Charlot, J. Dillet, L.F. Castanheira, G. Maranzana, L. Dubau, F. Maillard, M. Chatenet, O. Lottin, Environmental Degradation heterogeneities induced by repetitive start/stop events in proton exchange membrane fuel cell : Inlet vs . outlet and channel vs . land. Appl. Catal. B Environ. **138–139**, 416 (2013)
9. S. Abbou, J. Dillet, D. Spernjak, R. Mukundan, R.L. Borup, G. Maranzana, O. Lottin, High potential excursions during PEM fuel cell operation with dead-ended anode. J. Electrochem. Soc. **162**(10), F1212–F1220 (2015)

10. C.A. Reiser, L. Bregoli, T.W. Patterson, J.S. Yi, J.D.L. Yang, M.L. Perry, T.D. Jarvi, A reverse-current decay mechanism for fuel cells. Electrochem. Solid State Lett. **8**(6), A273 (2005)
11. H. Tang, Z. Qi, M. Ramani, J.F. Elter, PEM fuel cell cathode carbon corrosion due to the formation of air/fuel boundary at the anode. J. Power Sources **158**(2), 1306–1312 (2006)
12. K. Kinoshita, J. Bett, Potentiodynamic analysis of surface oxides on carbon blacks. Carbon **11**(4), 403–411 (1973)
13. S. Maass, F. Finsterwalder, G. Frank, R. Hartmann, C. Merten, Carbon support oxidation in PEM fuel cell cathodes. J. Power Sources **176**(2), 444–451 (2008)
14. J. Willsau, J. Heitbaum, The influence of Pt-activation on the corrosion of carbon in gas diffusion electrodes—A dems study. J. Electroanal. Chem. Interfacial Electrochem. **161**(1), 93–101 (1984)
15. L.M. Roen, C.H. Paik, T.D. Jarvic, Electrocatalytic corrosion of carbon support in PEMFC cathodes. Electrochem. Solid State Lett. **7**(1), A19 (2004)
16. L. Dubau, L. Castanheira, M. Chatenet, F. Maillard, J. Dillet, G. Maranzana, S. Abbou, O. Lottin, G. De Moor, A. El Kaddouri, C. Bas, L. Flandin, E. Rossinot, N. Caqué, Carbon corrosion induced by membrane failure: the weak link of PEMFC long-term performance. Int. J. Hydrog. Energy **39**(36), 21902–21914 (2014)
17. L. Dubau, L. Castanheira, F. Maillard, M. Chatenet, O. Lottin, G. Maranzana, J. Dillet, A. Lamibrac, J.C. Perrin, E. Moukheiber, A. Elkaddouri, G. De Moor, C. Bas, L. Flandin, N. Caqué, A review of PEM fuel cell durability: Materials degradation, local heterogeneities of aging and possible mitigation strategies. Wiley Interdiscip. Rev. Energy Environ. **3**, 540 (2014)
18. S.D. Knights, K.M. Colbow, J. St-Pierre, D.P. Wilkinson, Aging mechanisms and lifetime of PEFC and DMFC. J. Power Sources **127**(1–2), 127–134 (2004)
19. B. Wickman, H. Gronbeck, P. Hanarp, B. Kasemo, Corrosion induced degradation of Pt/C model electrodes measured with electrochemical quartz crystal microbalance. J. Electrochem. Soc. **157**(4), B592 (2010)
20. S.C. Ball, S.L. Hudson, D. Thompsett, B. Theobald, An investigation into factors affecting the stability of carbons and carbon supported platinum and platinum/cobalt alloy catalysts during 1.2V potentiostatic hold regimes at a range of temperatures. J. Power Sources **171**(1), 18–25 (2007)
21. K. Schlogl, K.J.J. Mayrhofer, M. Hanzlik, M. Arenz, Identical-location TEM investigations of Pt/C electrocatalyst degradation at elevated temperatures. J. Electroanal. Chem. **662**(2), 355–360 (2011)
22. L. Dubau, L. Castanheira, G. Berthomé, F. Maillard, An identical-location transmission electron microscopy study on the degradation of Pt/C nanoparticles under oxidizing, reducing and neutral atmosphere. Electrochim. Acta **110,** 273-281 (2013)
23. V. Parry, E. Appert, J.-C. Joud, Characterisation of wettability in gas diffusion layer in proton exchange membrane fuel cells. Appl. Surf. Sci. **256**(8), 2474–2478 (2010)
24. K.H. Radeke, K.O. Backhaus, A. Swiatkowski, Electrical conductivity of activated carbons. Carbon **29**(1), 122–123 (1991)
25. M. Polovina, B. Babić, B. Kaluderović, A. Dekanski, Surface characterization of oxidized activated carbon cloth. Carbon **35**(8), 1047–1052 (1997)
26. W. Vielstich, H. A. Gasteiger, and H. Yokokawa, Handbook of fuel cells: fundamentals technology and applications: advances in electrocatalysis, materials, diagnostics and durability (John Wiley & Sons, 2009)
27. L. Li, Y. Xing, Electrochemical durability of carbon nanotubes in noncatalyzed and catalyzed oxidations. J. Electrochem. Soc. **153**(10), A1823 (2006)
28. Y. Shao, G. Yin, J. Zhang, Y. Gao, Comparative investigation of the resistance to electrochemical oxidation of carbon black and carbon nanotubes in aqueous sulfuric acid solution. Electrochim. Acta **51**(26), 5853–5857 (2006)
29. G.M. Swain, The use of CVD diamond thin films in electrochemical systems. Adv. Mater. **6**(5), 388–392 (1994)
30. L. Qu, Y. Liu, J.-B. Baek, L. Dai, Nitrogen-doped graphene as efficient metal-free electrocatalyst for oxygen reduction in fuel cells. ACS Nano **4**(3), 1321–1326 (2010)
31. L.T. Soo, K.S. Loh, A.B. Mohamad, W.R.W. Daud, W.Y. Wong, An overview of the electrochemical performance of modified graphene used as an electrocatalyst and as a catalyst support in fuel cells. Appl. Catal. A Gen. **497**, 198–210 (2015)
32. K.A. Wepasnick, B.A. Smith, K.E. Schrote, H.K. Wilson, S.R. Diegelmann, D.H. Fairbrother, Surface and structural characterization of multi-walled carbon nanotubes following different oxidative treatments. Carbon **49**(1), 24–36 (2011)
33. V. Datsyuk, M. Kalyva, K. Papagelis, J. Parthenios, D. Tasis, A. Siokou, I. Kallitsis, C. Galiotis, Chemical oxidation of multiwalled carbon nanotubes. Carbon **46**(6), 833–840 (2008)
34. P. Hernández-Fernández, M. Montiel, P. Ocón, J.L.G. de la Fuente, S. García-Rodríguez, S. Rojas, J.L.G. Fierro, Functionalization of multi-walled carbon nanotubes and application as supports for electrocatalysts in proton-exchange membrane fuel cell. Appl. Catal. B Environ. **99**(1–2), 343–352 (2010)
35. Y. Shao, G. Yin, Y. Gao, Understanding and approaches for the durability issues of Pt-based catalysts for PEM fuel cell. J. Power Sources **171**(2), 558–566 (2007)
36. X. Zhao, A. Hayashi, Z. Noda, K. Kimijima, I. Yagi, K. Sasaki, Evaluation of change in nanostructure through the heat treatment of carbon materials and their durability for the start/stop operation of polymer electrolyte fuel cells. Electrochim. Acta **97**, 33–41 (2013)
37. K. Kinoshita, *Carbon: electrochemical and physicochemical properties* (John Wiley & Sons, New York, 1988)
38. S. Berthon-Fabry, L. Dubau, Y. Ahmad, K. Guérin, M. Chatenet, First insight into fluorinated Pt/carbon aerogels as more corrosion-resistant electrocatalysts for proton exchange membrane fuel cell cathodes. Electrocatalysis **6,** 521 (2015)
39. T. Asset, R. Chattot, F. Maillard, L. Dubau, Y. Ahmad, N. Batisse, M. Dubois, K. Guérin, F. Labbe, R. Metkemeijer, S. Berthon-Fabry, M. Chatenet, Activity and durability of platinum-based electrocatalysts supported on bare or fluorinated nanostructured carbon substrates. J. Electrochem. Soc. **165**(6), F3346–F3358 (2018)
40. E. Antolini, E.R. Gonzalez, Polymer supports for low-temperature fuel cell catalysts. Appl. Catal. A Gen. **365**(1), 1–19 (2009)
41. Z. Qi, P.G. Pickup, High performance conducting polymer supported oxygen reduction catalysts. Chem. Commun. **0**, 2299 (1998)
42. H. Meng, P.K. Shen, Tungsten carbide nanocrystal promoted Pt/C electrocatalysts for oxygen reduction. J. Phys. Chem. B **109**(48), 22705–22709 (2005)
43. O. Lori, S. Gonen, L. Elbaz, Highly active, corrosion-resistant cathode for fuel cells, based on platinum and molybdenum carbide. J. Electrochem. Soc. **164**(7), F825–F830 (2017)
44. S. Zhang, H. Zhu, H. Yu, J. Hou, B. Yi, P. Ming, The oxidation resistance of tungsten carbide as catalyst support for proton exchange membrane fuel cells. Chin. J. Catal. **28**(2), 109–111 (2007)
45. S. Yin, S. Mu, M. Pan, Z. Fu, A highly stable TiB2-supported Pt catalyst for polymer electrolyte membrane fuel cells. J. Power Sources **196**(19), 7931–7936 (2011)
46. S. Yin, S. Mu, H. Lv, N. Cheng, M. Pan, Z. Fu, A highly stable catalyst for PEM fuel cell based on durable titanium diboride support and polymer stabilization. Appl. Catal. B Environ. **93**(3–4), 233–240 (2010)

47. B. Avasarala, T. Murray, W. Li, P. Haldar, Titanium nitride nanoparticles based electrocatalysts for proton exchange membrane fuel cells. J. Mater. Chem. **19**(13), 1803 (2009)
48. Y. Xiao, G. Zhan, Z. Fu, Z. Pan, C. Xiao, S. Wu, C. Chen, G. Hu, Z. Wei, Titanium cobalt nitride supported platinum catalyst with high activity and stability for oxygen reduction reaction. J. Power Sources **284**, 296–304 (2015)
49. K.E. Fritz, P.A. Beaucage, F. Matsuoka, U. Wiesner, J. Suntivich, Mesoporous titanium and niobium nitrides as conductive and stable electrocatalyst supports in acid environments. Chem. Commun. **53**, 7250 (2017)
50. V.R. Stamenkovic, B. Fowler, B.S. Mun, G. Wang, P.N. Ross, C.A. Lucas, N.M. Marković, Improved oxygen reduction activity on Pt3Ni(111) via increased surface site availability. Science **315**(5811), 493–497 (2007)
51. S. Henning, L. Kühn, J. Herranz, J. Durst, T. Binninger, M. Nachtegaal, M. Werheid, W. Liu, M. Adam, S. Kaskel, A. Eychmüller, T.J. Schmidt, Pt-Ni aerogels as unsupported electrocatalysts for the oxygen reduction reaction. J. Electrochem. Soc. **163**(9), F998–F1003 (2016)
52. S. Henning, H. Ishikawa, L. Kühn, J. Herranz, E. Müller, A. Eychmüller, T.J. Schmidt, Angew. Unsupported Pt-Ni aerogels with enhanced high current performance and durability in fuel cell cathodes. Chem. - Int. Ed **56**, 10707 (2017)
53. S. Henning, L. Kühn, J. Herranz, M. Nachtegaal, R. Hübner, M. Werheid, A. Eychmüller, T.J. Schmidt, Effect of acid washing on the oxygen reduction reaction activity of Pt-Cu aerogel catalysts. Electrochim. Acta **233**, 210–217 (2017)
54. M. Oezaslan, F. Hasché, P. Strasser, PtCu3, PtCu and Pt3Cu alloy nanoparticle electrocatalysts for oxygen reduction reaction in alkaline and acidic media. J. Electrochem. Soc. **159**(4), B444–b454 (2012)
55. A. Bruix, A. Migani, G.N. Vayssilov, K.M. Neyman, J. Libuda, F. Illas, Effects of deposited Pt particles on the reducibility of CeO2(111). Phys. Chem. Chem. Phys. **13**(23), 11384 (2011)
56. T. Yu, J. Zeng, B. Lim, Y. Xia, aqueous-phase synthesis of Pt/CeO2 hybrid nanostructures and their catalytic properties. Adv. Mater. **22**(45), 5188–5192 (2010)
57. M. Wesselmark, B. Wickman, C. Lagergren, G. Lindbergh, Electrochemical performance and stability of thin film electrodes with metal oxides in polymer electrolyte fuel cells. Electrochim. Acta **55**(26), 7590–7596 (2010)
58. Y. Suzuki, A. Ishihara, S. Mitsushima, N. Kamiya, K. Ota, Sulfated-zirconia as a support of Pt catalyst for polymer electrolyte fuel cells. Electrochem. Solid State Lett. **10**(7), B105 (2007)
59. A.J. Martín, A.M. Chaparro, L. Daza, Single cell study of electrodeposited cathodic electrodes based on Pt–WO3 for polymer electrolyte fuel cells. J. Power Sources **196**(9), 4187–4192 (2011)
60. S.-Y. Huang, P. Ganesan, S. Park, B.N. Popov, Development of a titanium dioxide-supported platinum catalyst with ultrahigh stability for polymer electrolyte membrane fuel cell applications. J. Am. Chem. Soc. **131**(39), 13898–13899 (2009)
61. C. Beauger, L. Testut, S. Berthon-Fabry, F. Georgi, L. Guetaz, Doped TiO 2 aerogels as alternative catalyst supports for proton exchange membrane fuel cells: a comparative study of Nb, V and Ta dopants. Microporous Mesoporous Mater. **232**, 109–118 (2016)
62. K.-W. Park, K.-S. Seol, Nb-TiO2 supported Pt cathode catalyst for polymer electrolyte membrane fuel cells. Electrochem. Commun. **9**(9), 2256–2260 (2007)
63. T. Ioroi, Z. Siroma, N. Fujiwara, S. Yamazaki, K. Yasuda, Sub-stoichiometric titanium oxide-supported platinum electrocatalyst for polymer electrolyte fuel cells. Electrochem. Commun. **7**(2), 183–188 (2005)
64. T. Ioroi, H. Senoh, S.-I. Yamazaki, Z. Siroma, N. Fujiwara, K. Yasuda, Stability of corrosion-resistant magnéli-phase Ti_4O_7-supported PEMFC catalysts at high potentials. J. Electrochem. Soc. **155**(4), B321 (2008)
65. B. Seger, A. Kongkanand, K. Vinodgopal, P.V. Kamat, Platinum dispersed on silica nanoparticle as electrocatalyst for PEM fuel cell. J. Electroanal. Chem. **621**(2), 198–204 (2008)
66. H. Chhina, S. Campbell, O. Kesler, An oxidation-resistant indium tin oxide catalyst support for proton exchange membrane fuel cells. J. Power Sources **161**(2), 893–900 (2006)
67. Y. Takabatake, Z. Noda, S.M. Lyth, A. Hayashi, K. Sasaki, Cycle durability of metal oxide supports for PEFC electrocatalysts. Int. J. Hydrog. Energy **39**(10), 5074–5082 (2014)
68. Y.-C. Nah, I. Paramasivam, P. Schmuki, Doped TiO2 and TiO2 nanotubes: synthesis and applications. ChemPhysChem **11**(13), 2698–2713 (2010)
69. G. Ozouf, G. Cognard, F. Maillard, M. Chatenet, L. Guétaz, M. Heitzmann, P.A. Jacques, C. Beauger, Sb-doped SnO2aerogels based catalysts for proton exchange membrane fuel cells: Pt deposition routes, electrocatalytic activity and durability. J. Electrochem. Soc. **165**(6), F3036–F3044 (2018)
70. G. Ozouf, C. Beauger, Niobium- and antimony-doped tin dioxide aerogels as new catalyst supports for PEM fuel cells. J. Mater. Sci. **51**, 5305 (2016)
71. G. Cognard, G. Ozouf, C. Beauger, I. Jiménez-Morales, S. Cavaliere, D. Jones, J. Rozière, M. Chatenet, F. Maillard, Pt nanoparticles supported on niobium-doped tin dioxide: impact of the support morphology on Pt utilization and electrocatalytic activity. Electrocatalysis **8**(1), 51–58 (2017)
72. G. Cognard, G. Ozouf, C. Beauger, G. Berthomé, D. Riassetto, L. Dubau, R. Chattot, M. Chatenet, F. Maillard, Benefits and limitations of Pt nanoparticles supported on highly porous antimony-doped tin dioxide aerogel as alternative cathode material for proton-exchange membrane fuel cells. Appl. Catal. B Environ. **201**, 381–390 (2017)
73. G. Cognard, G. Ozouf, C. Beauger, L. Dubau, M. López-Haro, M. Chatenet, F. Maillard, Insights into the stability of Pt nanoparticles supported on antimony-doped tin oxide in different potential ranges. Electrochim. Acta **245**, 993–1004 (2017)
74. X. Liu, J. Chen, G. Liu, L. Zhang, H. Zhang, B. Yi, Enhanced long-term durability of proton exchange membrane fuel cell cathode by employing Pt/TiO2/C catalysts. J. Power Sources **195**(13), 4098–4103 (2010)
75. L. Timperman, Y.J. Feng, W. Vogel, N. Alonso-Vante, Substrate effect on oxygen reduction electrocatalysis. Electrochim. Acta **55**(26), 7558–7563 (2010)
76. B. Gao, C. Peng, G.Z. Chen, G. Li Puma, Photo-electro-catalysis enhancement on carbon nanotubes/titanium dioxide (CNTs/TiO2) composite prepared by a novel surfactant wrapping sol–gel method. Appl. Catal. B Environ. **85**(1–2), 17–23 (2008)
77. Z. Li, B. Gao, G.Z. Chen, R. Mokaya, S. Sotiropoulos, G. Li Puma, Carbon nanotube/titanium dioxide (CNT/TiO2) core–shell nanocomposites with tailored shell thickness, CNT content and photocatalytic/photoelectrocatalytic properties. Appl. Catal. B Environ. **110**, 50–57 (2011)
78. L. Xiong, A. Manthiram, Synthesis and characterization of methanol tolerant Pt/TiOx/C nanocomposites for oxygen reduction in direct methanol fuel cells. Electrochim. Acta **49**(24), 4163–4170 (2004)
79. Y. Bing, V. Neburchilov, C. Song, R. Baker, A. Guest, D. Ghosh, S. Ye, S. Campbell, J. Zhang, Effects of synthesis condition on formation of desired crystal structures of doped-TiO2/carbon composite supports for ORR electrocatalysts. Electrochim. Acta **77**, 225–231 (2012)
80. B. Ruiz Camacho, C. Morais, M.A. Valenzuela, N. Alonso-Vante, Enhancing oxygen reduction reaction activity and stability of platinum via oxide-carbon composites. Catal. Today **202**, 36–43 (2013)

81. K. Sasaki, L. Zhang, R.R. Adzic, Niobium oxide-supported platinum ultra-low amount electrocatalysts for oxygen reduction. Phys. Chem. Chem. Phys. **10**(1), 159–167 (2008)
82. D. Puthusseri, T.T. Baby, V. Bhagavathi Parambhath, R. Natarajan, R. Sundara, Carbon nanostructure grown using bimetal oxide as electrocatalyst support for proton exchange membrane fuel cell. Int. J. Hydrog. Energy **38**(15), 6460–6468 (2013)
83. Y. Chen, J. Wang, X. Meng, Y. Zhong, R. Li, X. Sun, S. Ye, S. Knights, Atomic layer deposition assisted Pt-SnO2 hybrid catalysts on nitrogen-doped CNTs with enhanced electrocatalytic activities for low temperature fuel cells. Int. J. Hydrog. Energy **36**(17), 11085–11092 (2011)
84. C. Du, M. Chen, X. Cao, G. Yin, P. Shi, A novel CNT@SnO2 core–sheath nanocomposite as a stabilizing support for catalysts of proton exchange membrane fuel cells. Electrochem. Commun. **11**(2), 496–498 (2009)
85. J. Jia, H. Wang, S. Ji, H. Yang, X. Li, R. Wang, SnO2-embedded worm-like carbon nanofibers supported Pt nanoparticles for oxygen reduction reaction. Electrochim. Acta **141**, 13–19 (2014)
86. J. Xu, D. Aili, Q. Li, C. Pan, E. Christensen, J.O. Jensen, W. Zhang, G. Liu, X. Wang, N.J. Bjerrum, Antimony doped tin oxide modified carbon nanotubes as catalyst supports for methanol oxidation and oxygen reduction reactions. J. Mater. Chem. A **1**(34), 9737 (2013)
87. S.J. Tauster, S.C. Fung, Strong metal-support interactions: occurrence among the binary oxides of groups IIA?VB. J. Catal. **55**(1), 29–35 (1978)
88. N. Kamiuchi, T. Matsui, R. Kikuchi, K. Eguchi, Nanoscopic observation of strong chemical interaction between Pt and Tin oxide. J. Phys. Chem. C **111**(44), 16470–16476 (2007)
89. C. Brieger, J. Melke, N. van der Bosch, U. Reinholz, H. Riesemeier, A. Guilherme Buzanich, M.K. Kayarkatte, I. Derr, A. Schökel, C. Roth, A combined in-situ XAS–DRIFTS study unraveling adsorbate induced changes on the Pt nanoparticle structure. J. Catal. **339**, 57–67 (2016)
90. S. Sharma, B.G. Pollet, Support materials for PEMFC and DMFC electrocatalysts—A review. J. Power Sources **208**, 96–119 (2012)
91. P.Y. You, S.K. Kamarudin, Recent progress of carbonaceous materials in fuel cell applications: An overview. Chem. Eng. J. **309**, 489 (2017)
92. P. Trogadas, T.F. Fuller, P. Strasser, Carbon as catalyst and support for electrochemical energy conversion. Carbon **75**, 5–42 (2014)
93. E. Antolini, E.R. Gonzalez, Tungsten-based materials for fuel cell applications. Appl. Catal. B Environ. **96**(3–4), 245–266 (2010)
94. E. Antolini, E.R. Gonzalez, Ceramic materials as supports for low-temperature fuel cell catalysts. Solid State Ionics **180**(9-10), 746–763 (2009)
95. F. Labbé, E. Disa, Y. Ahmad, K. Guérin, T. Asset, F. Maillard, M. Chatenet, R. Metkemeijer, S. Berthon-Fabry, Tin dioxide coated carbon materials as an alternative catalyst support for PEMFCs: Impacts of the intrinsic carbon properties and the synthesis parameters on the coating characteristics. Microporous Mesoporous Mater. **271**, 1–15 (2018)
96. H.-S. Oh, J.-G. Oh, Y.-G. Hong, H. Kim, Investigation of carbon-supported Pt nanocatalyst preparation by the polyol process for fuel cell applications. Electrochim. Acta **52**(25), 7278–7285 (2007)
97. R. Pekala, Organic aerogels from the polycondensation of resorcinol with formaldehyde. J. Mater. Sci. **24**(9), 3221–3227 (1989)
98. J. Marie, S. Berthon-Fabry, P. Achard, M. Chatenet, A. Pradourat, E. Chainet, Highly dispersed platinum on carbon aerogels as supported catalysts for PEM fuel cell-electrodes: comparison of two different synthesis paths. J. Non-Cryst. Solids **350**, 88–96 (2004)
99. W.Q. Han, A. Zettl, Coating single-walled carbon nanotubes with tin oxide. Nano Lett. **3**(5), 681–683 (2003)
100. J.C. Groen, L.A.A. Peffer, J. Pérez-Ramírez, Pore size determination in modified micro- and mesoporous materials. Pitfalls and limitations in gas adsorption data analysis. Microporous Mesoporous Mater. **60**(1–3), 1–17 (2003)
101. D.S. Knight, W.B. White, Characterization of diamond films by Raman spectroscopy. J. Mater. Res. **4**(02), 385–393 (1989)
102. A.C. Ferrari, J. Robertson, Interpretation of Raman spectra of disordered and amorphous carbon. Phys. Rev. B **61**(20), 14095–14107 (2000)
103. T. Asset, N. Job, Y. Busby, A. Crisci, V. Martin, V. Stergiopoulos, C. Bonnaud, A. Serov, P. Atanassov, R. Chattot, L. Dubau, F. Maillard, Porous hollow PtNi/C electrocatalysts: carbon support considerations to meet performance and stability requirements. ACS Catal. **8**(2), 893–903 (2018)
104. A.A.P.C.C. Herrmann, G.G. Perrault, Dual reference electrode for electrochemical pulse studies. Anal. Chem. **40**(7), 1173–1174 (1968)
105. L. Dubau, F. Maillard, Unveiling the crucial role of temperature on the stability of oxygen reduction reaction electrocatalysts. Electrochem. Commun. **63**, 65–69 (2016)
106. M.S. Wilson, F.H. Garzon, K.E. Sickafus, S. Gottesfeld, Surface area loss of supported platinum in polymer electrolyte fuel cells. J. Electrochem. Soc. **140**(10), 2872 (1993)
107. Y. Shao-Horn, P. J. Ferreira, O. La, D. Morgan, H. Gasteiger, R. Makharia, Coarsening of Pt nanoparticles in proton exchange membrane fuel cells upon potential cycling. ECS Transactions, **1**, 185 (2005)
108. M.S. Spencer, Models of strong metal-support interaction (SMSI) in Pt on TiO2 catalysts. J. Catal. **93**(2), 216–223 (1985)
109. B. Vion-Dury, M. Chatenet, L. Guetaz, F. Maillard, Determination of aging markers and their use as a tool to characterize Pt/C nanoparticles degradation mechanism in model PEMFC cathode environment. ECS Transactions, **41**, 697 (2011)